sustainability

MDPI

Article

Visible Domain Photocatalysis Performance of Ti-Si Thermal-Sprayed Coatings

Ionut Uncu, Ionut Claudiu Roata *, Catalin Croitoru * and Teodor Machedon-Pisu

Materials Engineering and Welding Department, Transilvania University of Brasov, Eroilor 29 Blvd., 500039 Brasov, Romania; ionutuncu@yahoo.com (I.U.); tmache@unitbv.ro (T.M.-P.)
* Correspondence: ionut.roata@unitbv.ro (I.C.R.); c.croitoru@unitbv.ro (C.C.)

Abstract: Cost and performance-effective materials used in advanced oxidation processes such as photocatalysis have obtained widespread attention in recent years. In this study, thermal spraying was used as a one-step method to obtain thick visible-light-active photocatalyst coatings on two types of substrates, namely, plain carbon steel and copper. A mixed metallic titanium–silicon powder bearing 10% wt. Si was used as feedstock. The optical bandgaps of the coatings were close to 1.000 eV, allowing good photodecoloration efficiencies (>89%) and mineralization efficiencies (>67%) for methylene blue dye from aqueous solutions under visible light irradiation. The photodegradation process could be successfully modelled by the Langmuir–Hinshelwood pseudo-first-order kinetic model, with reaction rate constants k between 0.16 and 1.06 h^{-1}.

Keywords: photocatalysis; thermal spraying; advanced oxidation processes; wastewater treatment

check for updates

Citation: Uncu, I.; Roata, I.C.; Croitoru, C.; Machedon-Pisu, T. Visible Domain Photocatalysis Performance of Ti-Si Thermal-Sprayed Coatings. *Sustainability* **2022**, *14*, 85. https://doi.org/10.3390/su14010085

Academic Editor: Changhyun Roh

Received: 3 December 2021
Accepted: 20 December 2021
Published: 22 December 2021

Publisher's Note: MDPI stays neutral with regard to jurisdictional claims in published maps and institutional affiliations.

Copyright: © 2021 by the authors. Licensee MDPI, Basel, Switzerland. This article is an open access article distributed under the terms and conditions of the Creative Commons Attribution (CC BY) license (https://creativecommons.org/licenses/by/4.0/).

1. Introduction

Nowadays, there are continuous efforts towards minimizing the environmental strain put on groundwaters by the continuous discharge of persistent organic compounds, which are challenging to be entirely degraded by conventional chemical or biochemical treatment methods [1,2].

Advanced oxidation processes (AOPs) such as heterogeneous photocatalysis involve the formation of highly reactive radicals, such as hydroxyl groups (OH) or superoxides (O_2^-), in an aqueous environment by the triggering of charge carriers (electrons and holes) separation on a semiconducting surface, irradiated with electromagnetic radiation from the UV or visible domain [3–5]. The hydroxyl radicals pose a very high standard redox potential (second to fluorine), thus presenting increased non-selective oxidation ability towards organic compounds [6].

With the aid of photocatalysts, trace amounts of various organic compounds, such as dyes, pesticides, drugs, or additives, could be efficiently neutralized from the point of view of their environmental impact [7,8]. While titanium dioxide (bandgap of ~3–3.2 eV) [9,10] and zinc oxide (bandgap of ~3.1–3.3 eV) [11,12] are by far the photocatalysts of choice, especially considering the vast amount of research put forward in the reference literature, an increased interest has been noted in the past ten years for doped TiO_2 or ZnO [13] or other photocatalytic material candidates, which are particularly capable of harvesting the visible portion of the electromagnetic spectrum [14,15].

There is still ongoing research to screen for economically efficient methods to synthesize photocatalyst materials that are easily up-scalable to be integrated at the industrial level, avoiding the well-known issues of photocatalytic (nano)powder handling, and to harvest the visible domain of the electromagnetic spectrum efficiently [16,17].

One of the promising techniques to obtain photocatalysts as coatings are represented by thermal spraying [18,19]. The thermal-spraying method (with all its technological sub-variants: flame spraying, plasma spraying, cold spraying, and high-velocity oxy-fuel spraying (HVOF)) is highly up-scalable, allows for the obtaining of thick coatings

(>50 mm) with a full pallet of chemical compositions (metal, ceramic, or hybrid coatings can be obtained), porosity, and roughness while being more economically efficient than other methods such as chemical vapour deposition (CVD) or physical vapour deposition (PVD) [20–22]. The principle of the thermal-spraying method is simple, involving heating, melting, or decomposing the precursor feedstock material (in powder, wire, solution, suspension, or slurry form), which is then impacted, plastically deformed, and anchored employing a carrier gas onto the substrate of interest [23,24].

This work aimed to test the suitability of flame spraying to obtain thick coatings, which could easily degrade methylene blue model dye from aqueous solutions by utilizing electromagnetic radiation from the visible domain. A Ti-Si powder with 10% wt. Si was used as feedstock material, while carbon steel, and copper, were used as potential widescale industrial substrates. The non-stoichiometric titanium oxides, prone to a high density of point defects, formed during the time-in-flight contact with atmospheric oxygen of the feedstock powder are especially beneficial for photocatalysis, as their bandgap is significantly lower than that of anatase or rutile polymorphs [25–27]. Additionally, titanium silicides such as $TiSi_2$ and Ti_5Si_3, which could form at high temperatures between the components of the feedstock powder, could have an excellent photocatalytic activity of splitting water into hydrogen and are very promising for application in solar panels [28].

Up to date, there have been no other reports on using this type of mixed feedstock powder to obtain photocatalyst coatings through thermal spraying or any other method. Some attempts have been to synthesize Ti-Si photocatalysts in microparticulate form by shock-wave-impacting Ti and Si powders [29] or in nanoparticulate form via the solvothermal method, with band gaps in the range of 2.5–2.8 eV [30].

The thermal-spraying process used in this study allowed for obtaining a stable, dense, and well-mechanically anchored coating. Its reproducible surface chemistry allows for a favourable mix between non-stoichiometric titanium oxides, silicon dioxide, and silicides, which is beneficial for photocatalysis.

2. Experimental

2.1. Materials

The titanium–silicon powder (10% wt. Si) with an average diameter of 115 µm was purchased from Oerlikon-Metco (Singapore). Electrolytic copper (99.5% Cu) and hipoeutectoid carbon 79 steel (1.0044-S273JR, EN 10025-2:2004) plates of 20 × 20 × 4 mm were used as substrate materials.

The methylene blue (MB) cationic dye ($C_{16}H_{18}ClN_3S$, M_w = 319.85), isopropyl alcohol, and ascorbic acid required for the photocatalysis experiments were purchased from Sigma-Aldrich (Burlington, MA, USA) and were of analytical grade (i.e., purity of minimum 99.5% wt. according to the manufacturer).

2.2. Coatings Obtaining

The flame spraying was performed using a CastoDyn DS8000 flame-spraying unit (Castolin Eutectic, Lausanne, Switzerland), using the following operational parameters: an acetylene pressure of 7×10^4 N m^{-2}, an oxygen pressure of 4×10^5 N m^{-2}, nitrogen carrier gas with a flow rate of 2.0 m^3/h, a powder feed rate of 0.7 g/min, and a standoff distance between the thermal spray nozzle and substrate of 200 mm. This distance was chosen since our prior experimental optimization trials proved it provides the best adherence to the substrate and lower porosity of the coatings. The substrate was preheated by the oxyacetylene flame (three successive passes and a substrate initial temperature ~200 °C) to improve the flattening of the feedstock powder at impact.

The samples' codes are St-TiSi (the carbon-steel-coated sample) and Cu-TiSi (the copper-coated sample).

2.3. Coatings Morphology and Structure

The cross-sectional morphology of the coatings was acquired using a Leica DLM inverted reflexion microscope, by grinding (P2500 grit) and polishing (alumina suspension, 3.5 µm) the resin-mounted samples. The etching of the samples was performed by immersing the samples top-down in aqua regia (1:3 vol. of concentrated HNO_3 to HCl) for 3 s, followed by washing with water and ethanol and hot-air drying.

The structural features of the coatings related to their composition and surface chemistry were assessed by X-ray diffraction (XRD) and X-ray photoelectron spectroscopy (XPS). A Bruker D8 Discover diffractometer (Billerica, MA, USA) using the Cu Kα line (8.04 keV) was used at a scanning speed of 0.06 degrees/s between 2θ values of 30 and 65°. For XPS, a Perkin–Elmer (Waltham, MA, USA) PHI 550 spectrometer was used, with the Al Kα line (1486.6 eV) as an X-ray source. Both survey spectra and narrow-scans of Ti2p and Si2p were acquired using a 20 eV pass energy.

The UV–VIS spectra of the coatings were acquired with a Perkin–Elmer (Waltham, MA, USA) Lambda 950 spectrophotometer (10 nm/min scan rate, integrating sphere).

The roughness profiles of the coatings before and after photocatalysis were determined with a TR-200 surface-roughness tester (NAMICON Testing, Otopeni, Romania).

2.4. Photocatalysis Performance

The photodegradation experiments were performed in glass beakers under static conditions. A stainless-steel custom-made closed cylindrical reactor containing four visible domain-emitting light bulbs (5700 K, wavelength distribution of ~400–750 nm), placed annular to the walls, was used to irradiate the samples placed in contact with 20 mL of an aqueous MB solution of 10^{-5} M initial concentration, at pH values of ~6.5. The irradiance value at the rim of the beaker containing the samples was 2 mW/cm^2. Each experiment was performed at an ambient temperature (22 °C) in duplicate, and the average value is presented in the article. Before irradiation, the samples were equilibrated in the dark in the MB solutions for ~4 h, and the equilibrium MB concentration was denoted as c_o.

Free-radical scavengers were added to the MB solutions in contact with the Cu-TiSi sample to determine the nature of the free radicals involved in the photodegradation. Isopropyl alcohol (IsoOH, 75 mL/20 mL of MB solution) was employed as a hydroxyl radical scavenger and ascorbic acid (HAs, 30 mg/20 mL of MB solution) as peroxide/superoxide radicals scavenger [25].

In each experimental instance, a Spekol 11 mono-channel spectrophotometer (Carl Zeiss, Jena, Germany) was used to monitor the concentration of methylene blue at determined time intervals (c_t), based on absorbance readings of the MB solutions at their absorption maximum from λ = 665 nm. The photodegradation (photodecoloration) efficiencies (η) were calculated with Equation (1):

$$\eta = \frac{c_0 - c_t}{c_0} \cdot 100\ (\%) \quad (1)$$

To bear a complete picture on the mineralization of the model dye, not only based on its photodecoloration, the total organic carbon (*TOC*) of the solutions before (TOC_0) and after (TOC_f) photocatalysis in case of all coatings was determined with a Shimadzu TOC-5000A TOC analyzer (Shimadzu Corporation, Japan), and the mineralization efficiency (η_m) was calculated according to Equation (2):

$$\eta_m = \frac{TOC_0 - TOC_f}{TOC_0} \cdot 100\ (\%) \quad (2)$$

3. Results and Discussion

Figure 1a–d depict the morphology at different magnifications of the Ti-Si coatings deposited on copper and carbon-steel substrates, respectively. In both cases, thick and well-fused coatings were obtained, which is typical for this deposition technique. The

average thickness of the coatings was 336.41 mm for Cu-TiSi and 545.97 mm for St-TiSi, respectively (Figure 1). Due to the high thermal conductivity of copper, the thickness of the coatings obtained on this substrate were lower than steel due to the better flattening of the feedstock powders on this substrate.

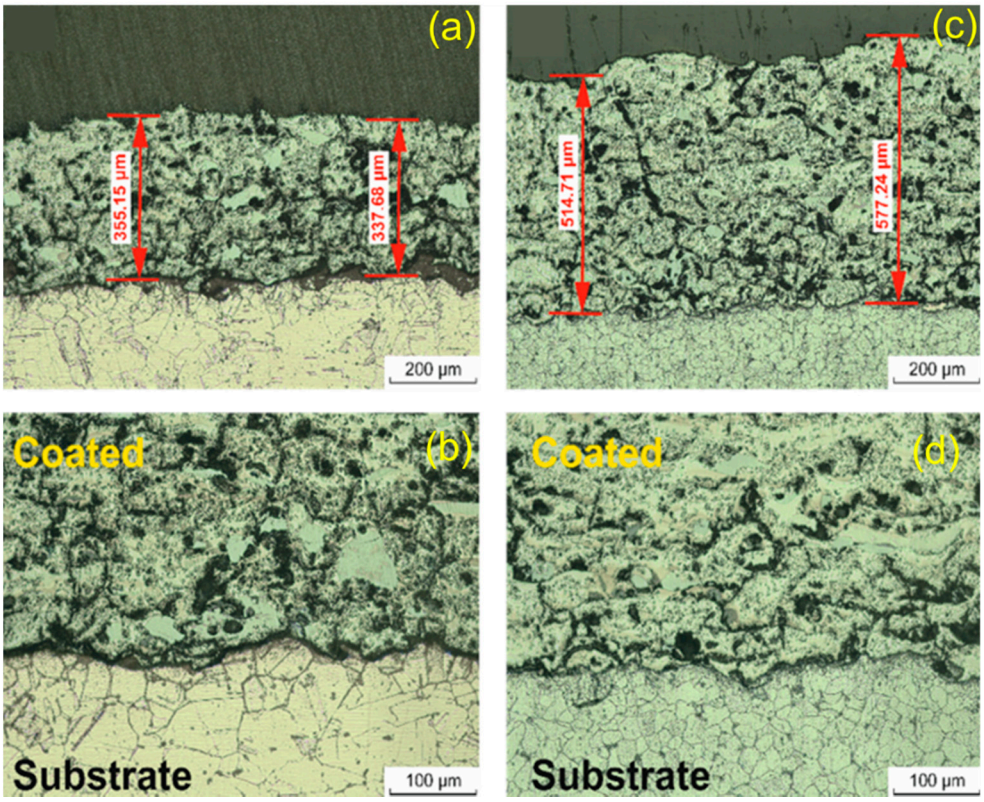

Figure 1. Cross-section optical microscopy of (**a**) Cu-TiSi (50×); (**b**) Cu-TiSi (100×); (**c**) St-TiSi (50×); and (**d**) St-TiSi (100×) samples.

Since the coatings are formed through local plastic deformation of the feedstock powder heated by the enthalpic source (oxyacetylene flame) when impacted on the substrate, their typical morphology is formed of overstacked layers (splats) of lamellar form. These splats could be observed in Figure 1a,b for the Cu-TiSi coatings and Figure 1c,d for the St-TiSi coatings. A more-compact coating was observed in the case of the copper substrate (Figure 1a vs. Figure 1c for steel)

Some dark areas on the splats' margins could be attributed to oxides (oxidation of Ti and Si during the powder time-of-flight) or different phases formed at high temperatures between the two phases coming in contact (Ti and Si). Both XRD and XPS spectroscopy results confirmed oxides and intermetallic phases (Figures 2 and 3), their presence being a well-known morphological feature of this TS technique [24,31,32]. Locally, some less perfectly flatted splats arising from incomplete melting of the feedstock could disturb the flat appearance of layers, contributing to the porosity of the coating (perpendicular to the spraying direction) [33]. Figure 1b (Cu-TiSi) and Figure 1d (St-TiSi) can be better observed in the higher magnification micrographs. Comparatively, the coating deposited on coper presented the highest number of non-metallic phases (oxides and silicides) than in the case of steel, consistent with the spectroscopy observations.

According to the Ti-Si phase diagram [34], the coating is expected to be composed from a mixture of α-Ti, Si, and titanium silicides, which was also observed from the XRD diffractograms of the sample, presented in Figure 2.

It can be seen that the initial powder is a mechanical mixture between hexagonal close-packed α-Ti (CIF card #00-151-2547) and Si (CIF card #00-901-1656), with Ti_6O oxide

(CIF card #00-152-9955) being present on the surface of Ti due to adsorbed atmospheric oxygen [35]. No other phases (chemical compounds) were detected in the feedstock powder.

Due to its high-temperature enthalpic source, flame spraying promotes the reaction between the α-Ti and Si phases present in the powder, forming two silicides, namely, $TiSi_2$ (orthorhombic, CIF card #00-100-9012) and Ti_5Si_3 (hexagonal, CIF card #00-154-1130). The diffraction patterns of the two coatings are relatively similar because the operational parameters of the deposition process are identical.

Additionally, oxidation of the Ti and Si phase occurs, due to contact of the heated powders with atmospheric oxygen, with the formation of Ti_2O_3 oxide (CIF card # 00-900-8082) and SiO_2 (α-cristobalite, CIF card # 00-101-0954).

Ti_2O_3 (Ti^{3+}) could occur by the thermal reduction in TiO_2 in the presence of Si and metallic Ti since no TiO_2 could be detected from the XRD diffraction data, which could be attributed to either a low degree of crystallinity or to a high ratio of Ti_2O_3 to TiO_2 with Ti_2O_3 formed on the surface of TiO_2. Ti^{4+}'s presence was detected by XPS (Figure 3a–c and Table 1), which could confirm this mechanism of formation.

Table 1. Relative surface chemistry of the samples calculated from XPS spectra.

Sample	Relative Element Concentration (at. %)			Ti Chemical Species ($2p_{3/2}$) (rel. %)		Si Chemical Species (rel. %)	
	$Ti2p_{3/2}$	Si2p	O1s				
St-TiSi	70.5	17.1	12.4	Ti^0	75.3	Si^0	89.0
				Ti^{3+}	17.8	Ti-Si	1.8
				Ti^{4+} (TiO_2/Ti_xSi_y)	6.9	SiO_2	9.2
Cu-TiSi	70.8	16.4	12.8	Ti^0	73.2	Si^0	83.9
				Ti^{3+}	20.4	Ti-Si	3.7
				Ti^{4+} (TiO_2/Ti_xSi_y)	6.4	SiO_2	12.4

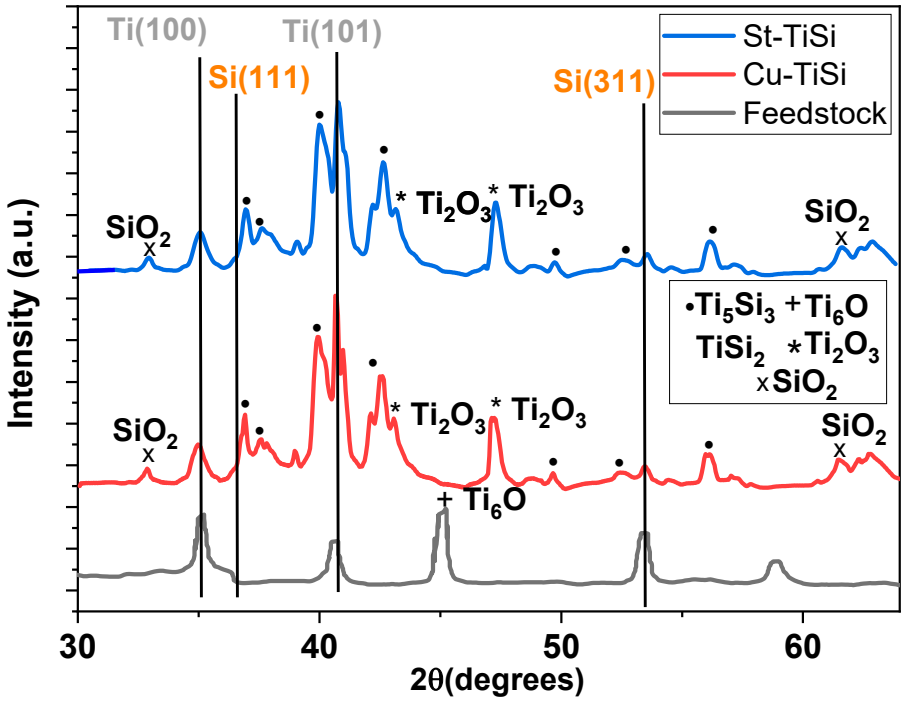

Figure 2. XRD spectra of Cu-TiSi and St-TiSi samples.

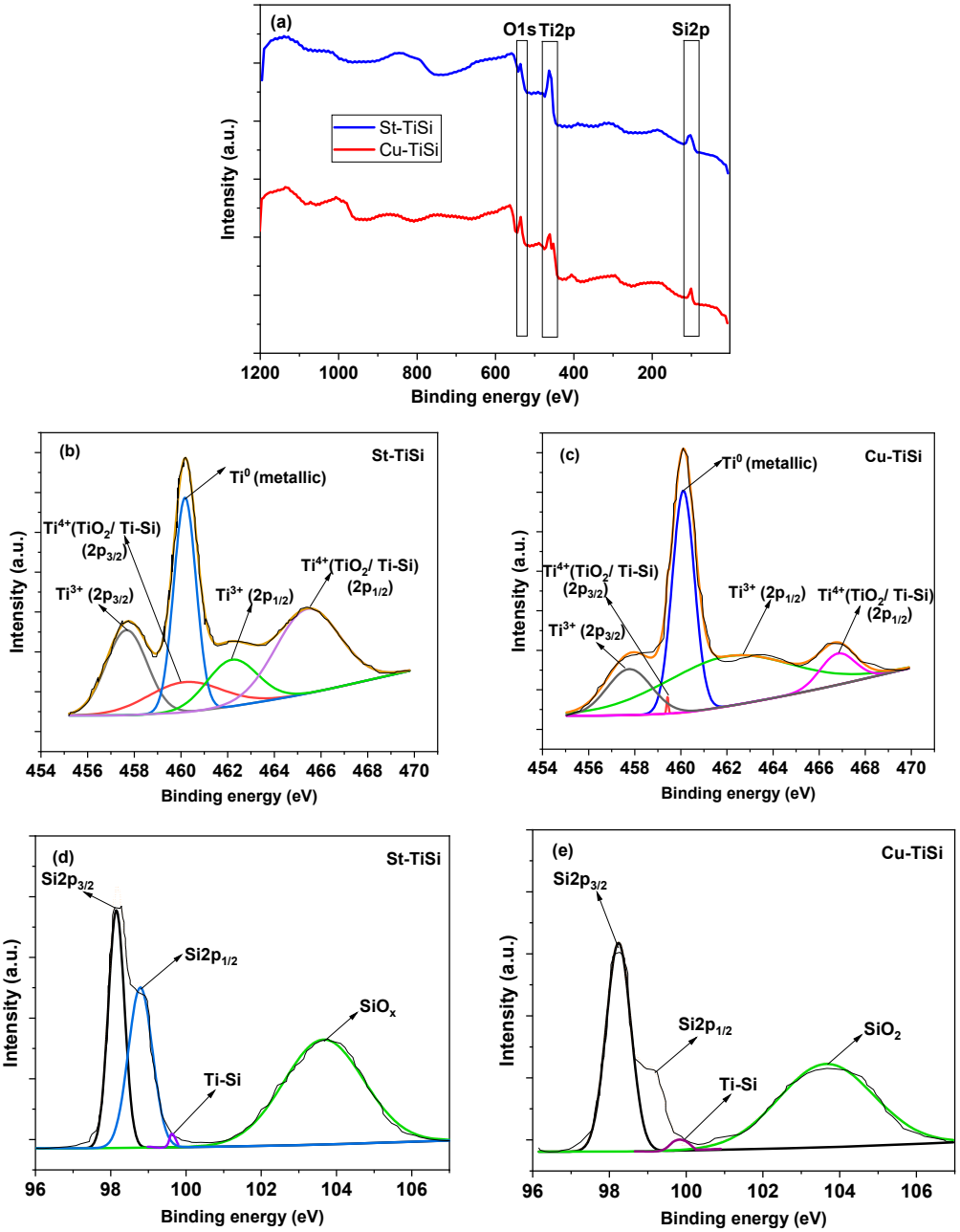

Figure 3. XPS spectra: (**a**) survey; (**b**,**c**) Ti2p envelopes; (**d**,**e**) Si2p envelopes of Cu-TiSi and St-TiSi samples.

Titanium (III) oxide, being a narrow band-gap semiconductor, has its energy level located between the conduction band and the valence band of TiO_2 [36]; it is therefore expected that electrons may be excited to the energy level of Ti_2O_3 from the valence band of TiO_2 or to the conduction band of TiO_2 from the energy level of Ti_2O_3 with visible light [37]. Although its presence could not be detected from either XRD or XPS, mixed Ti-Si oxides could also be formed in amounts lower than the detection limit of both these methods, which could also lead to a significant decrease in the energy band gap, synergic with the titanium silicides, and a more-efficient visible light harvesting in photocatalysis applications [38,39].

Figure 3a confirms the presence of Ti, O, and Si species on the surface of the thermal-sprayed samples. As it can be seen also from Table 1, the relative elemental distribution on the surface of the samples implies the presence of metallic Ti and Si, which constitute the majority elements in the coatings, as well as oxygen, which contributes to the formation of Ti^{4+} and Ti^{3+} oxides and SiO_2 (core-level envelopes of $Ti2p_{3/2}$ (~460.3 eV for Ti^{4+} and

~457.6 eV for Ti^{3+}) [40–43] and Si2p (~103.7 eV for Si^{4+} [42])) (Figure 3b–e). A relative amount of 1.8% and 3.7% of Ti–Si bonds were also detected in the Si2p core-level envelopes of Cu-TiSi and St-TiSi (Figure 3d,e), with the corresponding peaks centered at ~99.6 eV [42] confirming the presence of silicides in the surface chemistry of the samples.

Evidence on the visible-light-triggered photocatalytic activity could be depicted from the UV–VIS absorption spectra of the two coatings, presented in Figure 4a. It can be seen that a maximum absorption is present at ~451 nm (2.74 eV) for St-TiSi and at ~423 nm (2.93 eV) for Cu-TiSi.

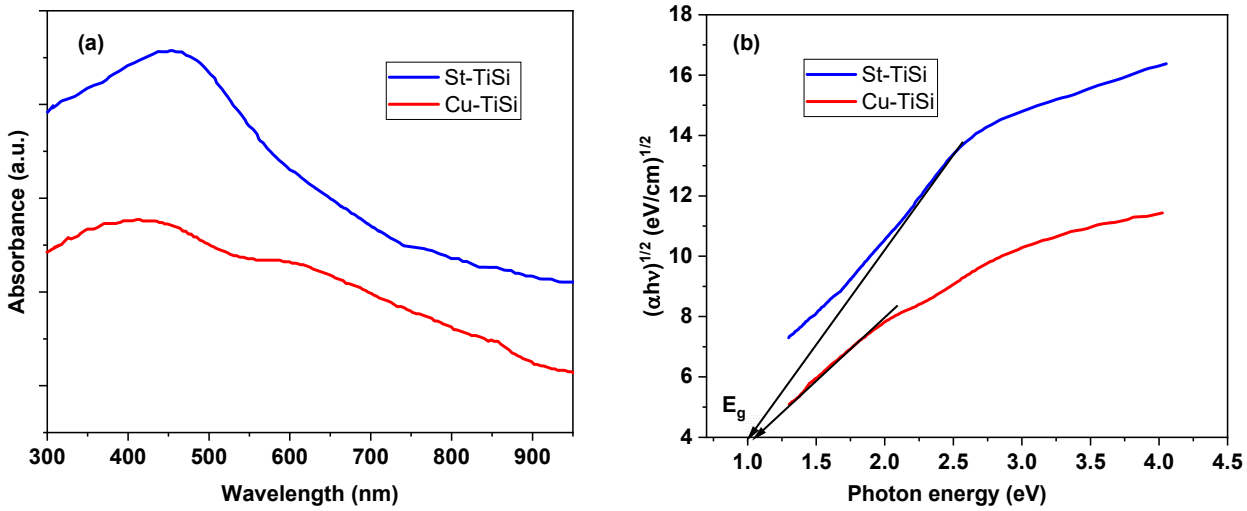

Figure 4. (**a**) UV–VIS spectra of St-TiSi and Cu-TiSi; (**b**) Tauc plots for determining E_g.

The UV–VIS spectra were used to determine the type of energy transition and the band gap energy E_g in the sprayed samples, using the Tauc plots. In building the Tauc plots, it was considered that the optical absorption coefficient α of the coatings depends on the photon energy ($h\nu$) according to Equation (3):

$$ln(\alpha h\nu) = ln\alpha_0 + n \cdot ln(h\nu - E_g) \quad (3)$$

where α_0 is the band tailing parameter, and n is the power factor of the transition mode (for direct allowed transitions, n = 0.5; for the forbidden transitions, n = 1.5; while for indirect allowed transitions, n = 2). For each sample, $ln(\alpha h\nu)$ was plotted as a function of $n{\cdot}ln(h\nu - E_g)$, yielding a straight line with the slope equal to the power factor n [44]. It was determined from such plots that the power factor n = 2 for both coatings, which means that they function as an indirect semiconductor (Table 2), similar to anatase and Ti_2O_3, which tend to have a higher compositional anisotropy related to the coordination of Ti ions and to the presence of oxygen vacancies [45,46].

Table 2. Parameters associated to the Tauc plots.

Sample	n	R^2	E_g (eV)
St-TiSi	1.994	0.997	1.083
Cu-TiSi	2.010	0.996	1.021

By plotting $(\alpha h\nu)^{1/2}$ as a function of the photon energy $h\nu$ for indirect transitions, the resulting dependency will have a linear part, whose extrapolation to the $h\nu$ axis gives the values for the optical-band gap energy [47,48].

Figure 5a depicts the photocatalysis kinetic efficiency, indicating high equilibrium values, namely, 89.50% for Cu-TiSi and 99.26% for St-TiSi. It could be concluded that, in the case of the coating deposited on steel, a concurrent photo-Fenton process could also occur, due to the formation of the Fe^{2+} ion from the oxidation of the metallic substrate.

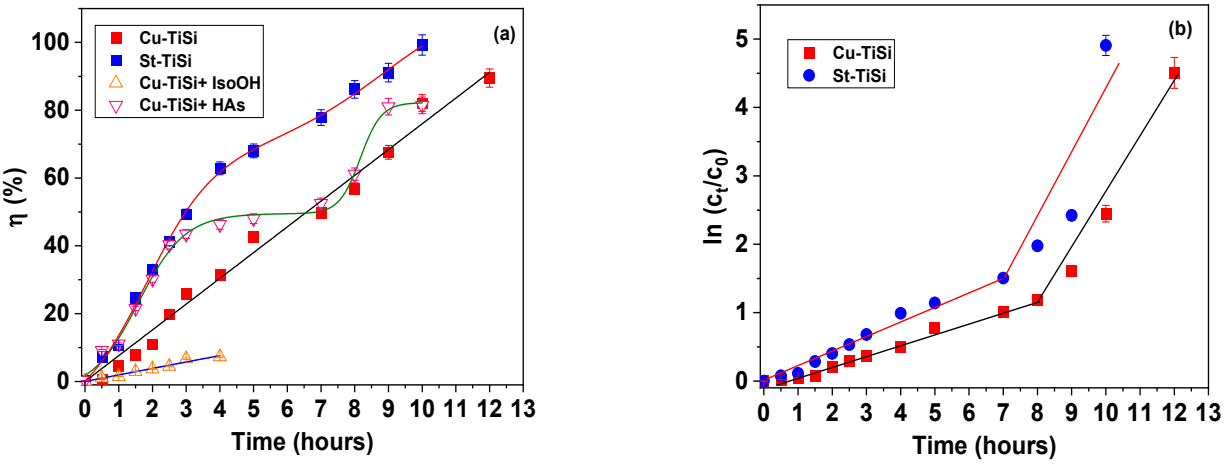

Figure 5. (**a**) Photocatalysis efficiency; (**b**) photo-Fenton degradation efficiency.

The addition of isopropyl alcohol (•OH radical scavenger) determines a significant decrease in the photocatalysis efficiency, evidencing the critical role of the hydroxyl radical in methylene blue degradation, possibly via Mechanism (4), where MBH denotes the methylene blue dye in its non-oxidized form and MB• the smaller molecular compounds, which could be formed during the initial stages of photodegradation [49,50]. Superoxide radicals seem to play a marginal role in the visible-light-aided degradation of MB since no significant decrease in the photocatalysis efficiency was registered by the addition of the ascorbic acid scavenger [51,52].

$$\begin{aligned} h^+ + H_2O &\overset{h\nu}{\rightleftharpoons} H^+ + \bullet OH \\ MBH + \bullet OH &\overset{h\nu}{\rightleftharpoons} MB\bullet + H_2O \end{aligned} \quad (4)$$

The photocatalysis process was modelled against the pseudo-first-order kinetic model (Figure 5b) proposed by Langmuir and Hinshelwood and depicted by Equation (5), where k signifies the pseudo-first-order rate constant [53].

$$ln\frac{c_t}{c_0} = k \cdot t \quad (5)$$

It could be observed that the photodegradation process of MB with the Ti-Si coating occurs in two distinct steps. The first one occurs with a slower onset (lower k_1 values) and could be ascribed to the photogeneration of the hydroxyl radicals, which initiate the degradation of the dye to higher-molecular compounds [54,55]. The second step occurs circa four times faster (constant rate k_2) and could imply the degradation of MB to smaller-molecular species.

The values of k_1 and k_2 are presented in Table 1, and the corresponding R^2 correlation coefficients are given in parenthesis after their actual values. The values depicted in Table 3 indicate the appropriateness of the kinetic model for modelling the experimental photocatalysis data.

For both coatings, good mineralization efficiencies were registered (Table 3), indicating the advanced oxidation of the dye and not its mere discoloration through the disruption of chromophore groups. Table 3 also indicates a decrease in the total roughness of both coating types after photocatalysis, probably due to micro-erosion.

Table 3. Mineralization efficiencies, pseudo-first-order rate constants of the photodecoloration process, and coatings' roughness profiles *.

Sample	η_m (%)	Total Roughness R_{tot} (μm)		Rate Constants			
		Before Photocatalysis	*After Photocatalysis*	k_1 (h^{-1})	R^2	k_2 (h^{-1})	R^2
Cu-TiSi	70.11 (±0.3)	28.4 (±0.4)	27.1 (±0.3)	0.16 (±0.02)	0.997	0.85 (±0.04)	0.986
St-TiSi	67.51 (± 0.4)	22.8 (±0.5)	20.3 (±0.4)	0.22 (±0.04)	0.991	1.06 (±0.03)	0.961

* Standard deviations are given in parenthesis.

4. Conclusions

This work aimed to enrich the international database in sustainable coatings capable of efficiently harvesting visible light to degrade trace amounts of pollutants from wastewaters. Through thermal flame spraying of mixed titanium–silicon feedstock powders, compact and adherent coatings were deposited on copper and carbon steels, which are two structural materials commonly employed in various installations in wastewater treatment plants.

High photodecoloration, mineralization efficiencies, and degradation rates were obtained, which were comparable to those presented in the reference literature for doped titania. The surface chemistry of the coatings, implying the presence of titanium (III) oxide and nonstoichiometric silicides (Ti_5Si_3 and $TiSi_2$), allows for the system's decreasing of the optical bandgap, which functions as an indirect semiconductor, near to 1.000 eV. Good preservation of the coatings surface roughness was registered after the photocatalysis, indicating good corrosion and erosion resistance.

Further studies will be performed to assess the lifecycle of the coatings and their performance in real-life wastewaters in the presence of interfering anions and cations.

Author Contributions: Conceptualization, C.C. and I.C.R.; methodology, C.C. and T.M.-P.; software, I.U., T.M.-P. and I.C.R.; validation, C.C. and I.C.R.; formal analysis, C.C. and I.U.; investigation, C.C., I.U. and T.M.-P.; resources, C.C.; data curation, I.U., I.C.R. and T.M.-P.; writing—original draft preparation, C.C. and I.C.R.; writing—review and editing, C.C. and T.M.-P.; visualization, I.C.R. and T.M.-P.; supervision, C.C.; project administration, C.C.; funding acquisition, C.C. All authors have read and agreed to the published version of the manuscript.

Funding: This research received no external funding.

Institutional Review Board Statement: Not applicable.

Informed Consent Statement: Not applicable.

Data Availability Statement: Not applicable.

Acknowledgments: The authors acknowledge the structural funds project PRO-DD (POS-CCE O.2.2.1, ID 123, SMIS 2637, ctr. No 11/2009) for providing the infrastructure used in this work at the CDI Institute of Transilvania University of Brasov.

Conflicts of Interest: The authors declare no conflict of interest.

References

1. Zhang, F.; Wang, X.; Liu, H.; Liu, C.; Wan, Y.; Long, Y.; Cai, Z. Recent Advances and Applications of Semiconductor Photocatalytic Technology. *Appl. Sci.* **2019**, *9*, 2489. [CrossRef]
2. Kumar, S.; Ahlawat, W.; Bhanjana, G.; Heydarifard, S.; Nazhad, M.M.; Dilbaghi, N. Nanotechnology-based water treatment strategies. *J. Nanosci. Nanotechnol.* **2014**, *14*, 1838–1858. [CrossRef] [PubMed]
3. Hu, Z.; Shi, J.; Yang, H.; Huang, J.; Sheng, F. How Organic Substances Promote the Chemical Oxidative Degradation of Pollutants: A Mini Review. *Sustainability* **2021**, *13*, 10993. [CrossRef]
4. Akurati, K.K.; Vital, A.; Dellemann, J.P.; Michalow, K.; Graule, T.; Ferri, D.; Baiker, A. Flame-made WO_3/TiO_2 nanoparticles: Relation between surface acidity, structure and photocatalytic activity. *Appl. Catal. B Environ.* **2008**, *79*, 53–62. [CrossRef]
5. Han, F.; Kambala, V.S.R.; Srinivasan, M.; Rajarathnam, D.; Naidu, R. Tailored titanium dioxide photocatalysts for the degradation of organic dyes in wastewater treatment: A review. *Appl. Catal. A Gen.* **2009**, *359*, 25–40. [CrossRef]

6. De-Nasri, S.J.; Nagarajan, S.; Robertson, P.K.J.; Ranade, V.V. Quantification of hydroxyl radicals in photocatalysis and acoustic cavitation: Utility of coumarin as a chemical probe. *Chem. Eng. J.* **2021**, *420*. [CrossRef]
7. Athanasekou, C.P.; Likodimos, V.; Falaras, P. Recent developments of TiO_2 photocatalysis involving advanced oxidation and reduction reactions in water. *J. Environ. Chem. Eng.* **2018**, *6*. [CrossRef]
8. Siwińska-Ciesielczyk, K.; Andrzejczak, A.; Paukszta, D.; Piasecki, A.; Moszyński, D.; Zgoła-Grześkowiak, A.; Jesionowski, T. Synthesis of selected mixed oxide materials with tailored photocatalytic activity in the degradation of tetracycline. *Materials* **2021**, *14*, 5361. [CrossRef]
9. Ansari, S.A.; Cho, M.H. Highly Visible Light Responsive, Narrow Band gap TiO_2 Nanoparticles Modified by Elemental Red Phosphorus for Photocatalysis and Photoelectrochemical Applications. *Sci. Rep.* **2016**, *6*, 25405. [CrossRef]
10. Fauzi, A.A.; Jalil, A.A.; Mohamed, M.; Naseri, N.A.; Hitam, C.N.C.; Khusnun, N.F.; Hassan, N.S.; Rahman, A.F.A.; Aziz, F.F.A.; Azmi, M.S.M. Fibrous silica induced narrow band gap TiO_2 catalyst for enhanced visible light-driven photodegradation of methylene blue. In Proceedings of the 8th Conference on Emerging Energy & Process Technology 2019 (CONCEPT 2019), Kuala Lumpur, Malaysia, 27–28 November 2019.
11. Sáenz-Trevizo, A.; Amézaga-Madrid, P.; Pizá-Ruiz, P.; Antúnez-Flores, W.; Miki-Yoshida, M. Optical band gap estimation of ZnO nanorods. *Mater. Res.* **2016**, *19*, 33–38. [CrossRef]
12. Ovando-Medina, V.M.; Farías-Cepeda, L.; Pérez-Aguilar, N.V.; Rivera de la Rosa, J.; Martínez-Gutiérrez, H.; Romero Galarza, A.; Cervantes-González, E.; Cayetano-Castro, N. Facile synthesis of low band gap ZnO microstructures. *Rev. Mex. Ing. Química* **2018**, *17*, 455–462. [CrossRef]
13. Dette, C.; Pérez-Osorio, M.A.; Kley, C.S.; Punke, P.; Patrick, C.E.; Jacobson, P.; Giustino, F.; Jung, S.J.; Kern, K. TiO_2 anatase with a bandgap in the visible region. *Nano Lett.* **2014**, *14*, 6533–6538. [CrossRef] [PubMed]
14. Liu, Y.; Huang, J.; Feng, X.; Li, H. Thermal-Sprayed Photocatalytic Coatings for Biocidal Applications: A Review. *J. Therm. Spray Technol.* **2021**, *30*, 1–24. [CrossRef]
15. Chitra, M.; Mangamma, G.; Uthayarani, K.; Neelakandeswari, N.; Girija, E.K. Band gap engineering in ZnO based nanocomposites. *Phys. E Low-Dimens. Syst. Nanostruct.* **2020**, *119*, 113969. [CrossRef]
16. Zeng, Y.; Wu, W.; Juntao, L.; Gao, J.; Chuanxian, D. Photo-decomposition property of thermal sprayed TiO_2 coatings. *Mater. Sci. Forum* **2006**, *510*, 26–29.
17. Kim, T.; Lee, M.; Lee, S.; Park, Y.; Jung, C.; Boo, J.-H. Development of surface coating technology of TiO_2 powder and improvement of photocatalytic activity by surface modification. *Thin Solid Films* **2005**, *475*, 171–177. [CrossRef]
18. Toma, F.-L.; Bertrand, G.; Klein, D.; Meunier, C.; Begin, S. Development of Photocatalytic Active TiO_2 Surfaces by Thermal Spraying of Nanopowders. *J. Nanomater.* **2008**, *2008*, 384171. [CrossRef]
19. Stengl, V.; Ageorges, H.; Ctibor, P.; Murafa, N. Atmospheric plasma sprayed (APS) coatings of Al_2O_3–TiO_2 system for photocatalytic application. *Photochem. Photobiol. Sci.* **2009**, *8*, 733–738. [CrossRef]
20. Roata, I.C.; Croitoru, C.; Pascu, A.; Stanciu, E.M. Photocatalytic coatings via thermal spraying: A mini-review. *AIMS Mater. Sci.* **2019**, *6*, 335–353. [CrossRef]
21. Roată, I.C.; Croitoru, C.; Pascu, A.; Stanciu, E.M. Photocatalytic performance of copper-based coatings deposited by thermal spraying. *J. Mater. Sci. Mater. Electron.* **2018**, *29*, 11345–11357. [CrossRef]
22. Winnicki, M.; Łatka, L.; Jasiorski, M.; Baszczuk, A. Mechanical properties of TiO_2 coatings deposited by low pressure cold spraying. *Surf. Coat. Technol.* **2021**, *405*, 126516. [CrossRef]
23. Sunitha, K.; Vasudev, H. A short note on the various thermal spray coating processes and effect of post-treatment on Ni-based coatings. *Mater. Today Proc.* 2021, *in press*. [CrossRef]
24. Gan, J.A.; Berndt, C.C. Thermal spray forming of titanium and its alloys. *Titan. Powder Metall.* **2015**, 425–446. [CrossRef]
25. Croitoru, C.; Roata, I.C.; Pascu, A.; Stanciu, E.M.; Hulka, I.; Stoian, G.; Lupu, N. Photocatalytic surfaces obtained through one-step thermal spraying of titanium. *Appl. Surf. Sci.* **2020**, *504*, 144173. [CrossRef]
26. Rasalingam, S.; Kibombo, H.S.; Wu, C.-M.; Budhi, S.; Peng, R.; Baltrusaitis, J.; Koodali, R. Influence of Ti–O–Si hetero-linkages in the photocatalytic degradation of Rhodamine B. *Catal. Commun.* **2013**, *31*, 66–70. [CrossRef]
27. Valeeva, A.A.; Kozlova, E.A.; Vokhmintsev, A.S.; Kamalov, R.V.; Dorosheva, I.B.; Saraev, A.A.; Weinstein, I.A.; Rempel, A.A. Nonstoichiometric titanium dioxide nanotubes with enhanced catalytical activity under visible light. *Sci. Rep.* **2018**, *8*, 9607. [CrossRef] [PubMed]
28. Liu, J.; Zhang, H.; Chen, P.; Cui, N.; Gao, X. Ti-Si photocatalyst for producing hydrogen synthesized by shock wave. In Proceedings of the Conference of the American Physical Society Topical Group on Shock Compression of Condensed Matter, Chicago, IL, USA, 26 June–1 July 2011; Volume 1426, pp. 1403–1406.
29. Hokamoto, K.; Lee, S.H.; Lee, J.S.; Tanaka, S.; Mori, A.; Tomoshige, R.; Fujita, M. Characteristics of the surface coating layer obtained by shock compaction and reaction synthesis through underwater shock compression. *Sci. Technol. Energ. Mater.* **2005**, *66*, 351.
30. Dai, Y.; Yin, L. Synthesis and photocatalytic activity of Ag–Ti–Si ternary modified α-Bi_2O_3 nanoporous spheres. *Mater. Lett.* **2015**, *142*, 225–228. [CrossRef]
31. Hu, W.; Markovych, S.; Tan, K.; Shorinov, O.; Cao, T. Research on wear resistance coating of aircraft titanium alloy parts by cold spraying technology. *Aerosp. Tech. Technol.* **2020**, 61–71. [CrossRef]

32. Pacheco, M.Y.F.; Galvis, F.V.; Lopez, E.V.; Téllez, C.M.M.; Rodríguez, G.P. Evaluation of morphology, wear and corrosion resistance of ZrO_2-Al_2O_3/Ni coatings deposited on carbon steel substrates with flame spraying. *Ingeniare. Rev. Chil. Ing.* **2017**, *25*, 721–732. [CrossRef]
33. Richter, A.; Berger, L.M.; Sohn, Y.J.; Conze, S.; Sempf, K.; Vaßen, R. Impact of Al_2O_3-40 wt.% TiO_2 feedstock powder characteristics on the sprayability, microstructure and mechanical properties of plasma sprayed coatings. *J. Eur. Ceram. Soc.* **2019**, *39*, 5391–5402. [CrossRef]
34. Gröbner, J.; Mirković, D.; Schmid-Fetzer, R. Thermodynamic aspects of grain refinement of Al–Si alloys using Ti and B. *Mater. Sci. Eng. A* **2005**, *395*, 10–21. [CrossRef]
35. Zhong, X.; Xu, M.; Yang, L.; Qu, X.; Yang, L.; Zhang, M.; Liu, H.; Ma, Y. Predicting the structure and stability of titanium oxide electrides. *npj Comput. Mater.* **2018**, *4*, 4. [CrossRef]
36. Liu, H.; Yang, W.; Ma, Y.; Yao, J. Extended visible light response of binary TiO_2-Ti_2O_3 photocatalyst prepared by a photo-assisted sol–gel method. *Appl. Catal. A Gen.* **2006**, *299*, 218–223. [CrossRef]
37. Cacciafesta, P.; Hallam, K.R.; Oyedepo, C.A.; Humphris, A.D.L.; Miles, M.; Jandt, K.D. Characterization of Ultraflat Titanium Oxide Surfaces. *Chem. Mater.* **2002**, *14*, 777–789. [CrossRef]
38. Sun, R.; Chen, Z.; Yang, Y.; Peng, J.; Zheng, T. Effects and mechanism of SiO_2 on photocatalysis and super hydrophilicity of TiO_2 films prepared by sol-gel method. *Mater. Res. Express* **2018**, *6*, 046409. [CrossRef]
39. Hakki, A.; Yang, L.; Wang, F.; Macphee, D.E. The Effect of Interfacial Chemical Bonding in TiO_2-SiO_2 Composites on Their Photocatalytic NOx Abatement Performance. *J. Vis. Exp.* **2017**, e56070. [CrossRef]
40. Chinh, V.D.; Broggi, A.; Di Palma, L.; Scarsella, M.; Speranza, G.; Vilardi, G.; Thang, P.N. XPS Spectra Analysis of Ti^{2+}, Ti^{3+} Ions and Dye Photodegradation Evaluation of Titania-Silica Mixed Oxide Nanoparticles. *J. Electron. Mater.* **2018**, *47*, 2215–2224. [CrossRef]
41. Su, J.; Zou, X.; Chen, J.-S. Self-modification of titanium dioxide materials by Ti^{3+} and/or oxygen vacancies: New insights into defect chemistry of metal oxides. *RSC Adv.* **2014**, *4*, 13979–13988. [CrossRef]
42. Brassard, D.; Sarkar, D.K.; El Khakani, M.A.; Ouellet, L. Tuning the electrical resistivity of pulsed laser deposited $TiSiO_x$ thin films from highly insulating to conductive behaviors. *Appl. Phys. Lett.* **2004**, *84*, 2304. [CrossRef]
43. Cho, J.; Debucquoy, M.; Payo, M.R.; Schapmans, E.; Gordon, I.; Szlufcik, J.; Poortmans, J. Evidence of TiOx reduction at the SiOx/TiOx interface of passivating electron-selective contacts. In Proceedings of the SILICONPV 2018, the 8th International Conference on Crystalline Silicon Photovoltaics, Lausanne, Switzerland, 19–21 March 2018; Volume 1999.
44. Perez, I.; Carrejo, J.L.E.; Sosa, V.; Perera, F.G.; Mancillas, J.R.F.; Galindo, J.T.E.; Rodríguez, C.I.R. Evidence for structural transition in crystalline tantalum pentoxide films grown by RF magnetron sputtering. *J. Alloys Compd.* **2017**, *712*, 303–310. [CrossRef]
45. Sanjinés, R.; Tang, H.; Berger, H.; Gozzo, F.; Margaritondo, G.; Lévy, F. Electronic structure of anatase TiO_2 oxide. *J. Appl. Phys.* **1994**, *75*, 2945–2951. [CrossRef]
46. Singh, V.; Pulikkotil, J. Electronic phase transition and transport properties of Ti_2O_3. *J. Alloys Compd.* **2016**, *658*, 430–434. [CrossRef]
47. Hassanien, A.S.; Akl, A.A. Influence of composition on optical and dispersion parameters of thermally evaporated non-crystalline Cd50S50−xSex thin films. *J. Alloys Compd.* **2015**, *648*, 280–290. [CrossRef]
48. Cristea, D.; Cunha, L.; Gabor, C.; Ghiuta, I.; Croitoru, C.; Marin, A.; Velicu, L.; Besleaga, A.; Vasile, B. Tantalum Oxynitride Thin Films: Assessment of the Photocatalytic Efficiency and Antimicrobial Capacity. *Nanomaterials* **2019**, *9*, 476. [CrossRef]
49. Ramar, V.; Balasubramanian, K. Reduced Graphene Oxide/WO_3 Nanorod Composites for Photocatalytic Degradation of Methylene Blue under Sunlight Irradiation. *ACS Appl. Nano Mater.* **2021**, *4*, 5512–5521. [CrossRef]
50. Nguyen, V.H.; Bui, Q.T.P.; Vo, D.-V.N.; Lim, K.T.; Bach, L.G.; Do, S.T.; Van Nguyen, T.; Doan, V.-D.; Nguyen, T.-D.; Nguyen, T.D. Effective Photocatalytic Activity of Sulfate-Modified $BiVO_4$ for the Decomposition of Methylene Blue Under LED Visible Light. *Materials* **2019**, *12*, 2681. [CrossRef]
51. Neto, N.A.; Dias, B.; Tranquilin, R.; Longo, E.; Li, M.; Bomio, M.; Motta, F. Synthesis and characterization of Ag^+ and Zn^{2+} co-doped $CaWO_4$ nanoparticles by a fast and facile sonochemical method. *J. Alloys Compd.* **2020**, *823*, 153617. [CrossRef]
52. Tang, J.; Shi, Y.; Cai, W.; Liu, F. Construction of Embedded Heterostructured $SrZrO_3$/Flower-like MoS_2 with Enhanced Dye Photodegradation under Solar-Simulated Light Illumination. *ACS Omega* **2020**, *5*, 9576–9584. [CrossRef]
53. Liu, B.; Zhao, X.; Terashima, C.; Fujishima, A.; Nakata, K. Thermodynamic and kinetic analysis of heterogeneous photoca-talysis for semiconductor systems. *Phys. Chem. Chem. Phys.* **2014**, *16*, 8751–8760. [CrossRef]
54. Xu, C.; Rangaiah, G.; Zhao, X.S. Photocatalytic Degradation of Methylene Blue by Titanium Dioxide: Experimental and Modeling Study. *Ind. Eng. Chem. Res.* **2014**, *53*, 14641–14649. [CrossRef]
55. Peter, A.; Mihaly-Cozmuta, A.; Nicula, C.; Mihaly-Cozmuta, L.; Jastrzębska, A.; Olszyna, A.; Baia, L. UV Light-Assisted Degradation of Methyl Orange, Methylene Blue, Phenol, Salicylic Acid, and Rhodamine B: Photolysis Versus Photocatalyis. *Water Air Soil Pollut.* **2017**, *228*, 41. [CrossRef]